Chinese Chemical Letters 36 (2025) 110347

Contents lists available at ScienceDirect

Chinese Chemical Letters

journal homepage: www.elsevier.com/locate/cclet

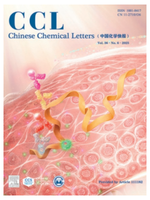

Electrocatalytic nitrate reduction on Fe, Fe_3O_4, and Fe@Fe_3O_4 cathodes: Elucidating structure-sensitive mechanisms of direct electron *versus* hydrogen atom transfer

Yuwei Liu, Yihui Zhu, Weijian Duan*, Yizhuo Yang, Haorui Tuo, Chunhua Feng*

The Key Lab of Pollution Control and Ecosystem Restoration in Industry Clusters, Ministry of Education, School of Environment and Energy, South China University of Technology, Guangzhou 510006, China

ARTICLE INFO

Article history:
Received 19 March 2024
Revised 18 July 2024
Accepted 16 August 2024
Available online 17 August 2024

Keywords:
Electrochemical nitrate reduction
Fe electrocatalysts
Electron transfer mechanism
Hydrogen atom
Ammonia synthesis

ABSTRACT

Electrochemical nitrate reduction (NO_3RR) offers a promising avenue for treating nitrate-contaminated water and recovering ammonia (NH_3), yet the complexities of direct electron transfer (DET) and hydrogen atom transfer (HAT) mechanisms crucial for efficiency remain elusive. This study bridges the gap with a combined experimental and theoretical approach, elucidating the impact of catalyst structure on NO_3RR pathways. We discover that catalysts favoring strong NO_3^- adsorption and efficient water dissociation were more inclined towards DET, enhancing denitrification. The Fe@Fe_3O_4/FF cathode, leveraging the synergistic interplay between metallic Fe and Fe_3O_4, excelled in NO_3RR *via* DET, achieving an NH_3 yield of 0.28 mmol h^{-1} cm^{-2} and a Faradaic efficiency of 95.7% for NH_3 at -1.6 V (*vs.* SCE), with minimal nitrite accumulation at 100 mmol/L nitrate. Conversely, the Fe/FF and Fe_3O_4/CC cathodes showed reduced NH_3 production and increased nitrite levels, attributed to the lack of Fe_3O_4 and metallic Fe, respectively, resulting in a dominant HAT mechanism. Moreover, Fe@Fe_3O_4/FF facilitated complete denitrification in real wastewater treatment by harnessing Cl^- for electrochemically mediated breakpoint chlorination. This research not only deepens our understanding of NO_3RR mechanisms but also paves the way for designing superior nitrate reduction catalysts.

Nitrate, a highly soluble and toxic pollutant, has been increasingly detected in various water sources, including agricultural runoff, industrial wastewater, and drinking water. This pollutant is directly linked to the adverse eutrophication phenomenon and other serious environmental issues that threaten both ecosystem balance and human health [1-3]. The development of highly effective denitrification strategies is desirable and receives considerable attention. Among these, the electrochemical nitrate reduction reaction (NO_3RR) emerges as a promising method to achieve this goal in a greener and more sustainable manner, due to the remarkable advantages of its renewable electricity-driven nature, application feasibility, and high efficiency [4-7]. Additionally, ammonia (NH_3), as the principal product during NO_3RR, has been widely proposed as the most potential candidate for a sustainable hydrogen energy carrier because of its high energy density (4.3 kW/kg) and economic affordability for storage and transport [8]. Therefore, the advancement of NO_3RR technology has gain increasing attention from both the environmental and energy communities.

Electrocatalysts play a crucial role in the emerging technology of nitrate reduction, as they significantly influence the activity and product distribution of NO_3RR. A wide range of materials with unique structures and compositions has been explored to enhance the NH_3 yield rate and Faradaic efficiency (FE) of NO_3RR, including pure metals (*e.g.*, Ru and Co) [9,10], metal alloys (*e.g.*, CuPd) [11-13], metal oxides (*e.g.*, Co_3O_4 and Fe_3O_4) [14,15], and carbon-based materials (*e.g.*, single atomic catalysts) [16-18]. Despite considerable progress in developing materials for NH_3 production *via* NO_3RR, the critical relationship between the structure of catalysts and their performance in NO_3RR remains unclear. This lack of clarity is due to insufficient understanding of the reaction process, which significantly impedes the rational design and advancement of catalysts for efficient NH_3 production. It is generally recognized that NO_3RR can proceed *via* either a direct electron transfer mechanism (DET) [19,20] or an indirect hydrogen atom ($^{\bullet}H$) transfer (HAT) mechanism [21,22], with each expected to lead to different NO_3RR performance. Previous studies have shown that a balance between the consumption and supply of $^{\bullet}H$ generated from the

---

* Corresponding authors.
E-mail addresses: 202310189796@mail.scut.edu.cn (W. Duan), chfeng@scut.edu.cn (C. Feng).

https://doi.org/10.1016/j.cclet.2024.110347

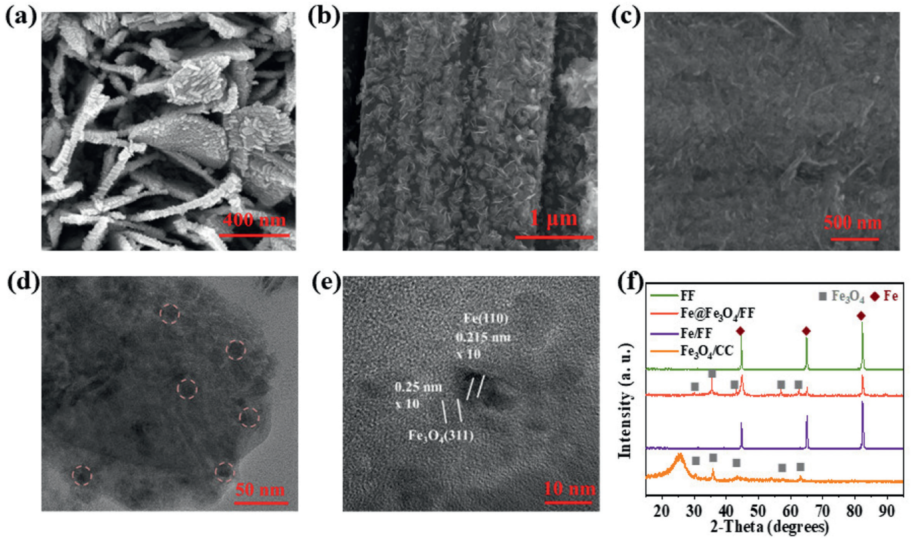

Fig. 1. SEM images of (a) Fe@Fe_3O_4/FF, (b) Fe_3O_4/CC, and (c) Fe/FF. (d, e) HRTEM images of Fe@Fe_3O_4/FF. (f) XRD patterns of three electrocatalysts.

Volmer step during the hydrogen evolution reaction (HER) within the HAT mechanism is critical for superior NH_3 yield *via* NO_3RR [23]. An excessive supply of $^{\bullet}H$ may lead to a preferred occurrence of competitive HER, thereby reducing the FE of NH_3. Theoretically, the DET mechanism does not involve hydrogen atoms as key intermediates for the parasitic HER, potentially leading to higher NO_3RR efficiency due to reduced $^{\bullet}H$ generation. The dominance of a particular mechanism is highly dependent on the catalyst property. Therefore, a comprehensive understanding of the intricate relationship between catalyst structure, reaction mechanism, and NO_3RR performance is of great importance.

Herein, we designed and fabricated three types of free-standing electrocatalysts, building upon our previous work with minor modifications [24]. These catalysts included pure metallic Fe nanoparticles *in-situ* grown on iron foil (denoted as Fe/FF), pure Fe_3O_4 nanosheets on carbon cloth (Fe_3O_4/CC), and a mixture of metallic Fe nanoparticles and Fe_3O_4 nanosheets *in-situ* constructed on iron foil (Fe@Fe_3O_4/FF). By carefully examining and comparing their NO_3RR performance in terms of NH_3 yield, NH_3 selectivity, and FE, we employed a combination of electrochemical characterizations, quenching experiments, electron spin resonance (ESR) measurements, and theoretical calculations to discern the differences in catalyst structure and reaction mechanisms. Through this comprehensive analysis, we were able to elucidate the structure-sensitive mechanisms of DET *versus* HAT and their impact on NO_3RR performance. This investigation provides valuable insights into catalyst design for the electrochemical treatment of nitrate-laden wastewater, offering an important perspective on optimizing the efficiency and selectivity of the NO_3RR process.

The experimental section is elaborated in Supporting information, which includes chemicals and reagents, preparation of catalysts, experimental setup, physicochemical and electrochemical characterizations, analysis methods, and density functional theory (DFT) calculations. The electrodes used in this study were fabricated using a similar method as described previously [24], which involved initial annealing in a static air atmosphere followed by electrochemical activation. Briefly, Fe@Fe_3O_4/FF was prepared by annealing Fe foil at 500 °C in a static air atmosphere, followed by electrochemical cathode activation at 10 mA/cm^2. Meanwhile, Fe/FF was produced using the same procedure but with the annealing temperature adjusted to 350 °C. A two-step protocol was employed for synthesizing Fe_3O_4/CC, which consisted of electrodeposition of $Fe(OH)_3$ on carbon cloth followed by air annealing at 350 °C. Physicochemical characterization techniques including scanning electron microscopy (SEM), transmission electron microscopy (TEM), and diffractometry (XRD) were utilized to identify differences in composition and structure among the Fe/FF, Fe_3O_4/CC, and Fe@Fe_3O_4/FF cathodes. Fig. 1a and Fig. S1 (Supporting information) illustrate that the surface of Fe@Fe_3O_4/FF appeared rougher in comparison to the smoother surface of Fe_3O_4/FF prior to electrochemical treatment, with a high density of nanoparticles dispersed on the original Fe_3O_4 nanosheets. This observation aligns with our previous findings that electrochemical reduction treatment facilitates the formation of Co nanoparticles from Co_3O_4 nanosheets on cobalt foil (CF) under the influence of an applied cathode potential [24]. Fig. 1b shows that Fe_3O_4/CC exhibited flat nanosheet morphology, similar to Fe_3O_4/FF before electrochemical treatment. A lower calcination temperature of 350 °C during Fe/FF synthesis resulted in fewer Fe_3O_4 nanosheets forming on FF (Fig. S2 in Supporting information), in contrast to the abundant and dense formation of Fe_3O_4 nanosheets on Fe_3O_4/FF (calcination at 500 °C), which were then entirely reduced to metallic Fe without any remaining Fe_3O_4 through the same electrochemical treatment, as depicted in Fig. 1c. Moreover, TEM analyses (Figs. 1d and e) further supported these findings, revealing lattice fringes with interplanar spacings of 0.25 nm and 0.215 nm, corresponding to the (311) plane of Fe_3O_4 and the (110) plane of Fe, respectively, indicating the coexistence of metallic Fe and Fe_3O_4 in Fe@Fe_3O_4/FF. However, for Fe_3O_4/CC, only Fe_3O_4 lattice fringes were observed (Fig. S3 in Supporting information). The composition of the three electrocatalysts was also confirmed through XRD analysis (Fig. 1f), where crystalline phases of Fe and Fe_3O_4 were identified for Fe/FF and Fe_3O_4/CC, respectively. In contrast, Fe@Fe_3O_4/FF exhibited crystalline phases of both Fe and Fe_3O_4, suggesting that Fe@Fe_3O_4/FF comprises both metallic Fe and Fe_3O_4 nanosheets.

To compare the effectiveness in nitrate removal and NH_3 production among the three specially prepared cathodes and a bare FF cathode, the chronoamperometry method was utilized for evaluation. Fig. S4 (Supporting information) reveals that after 6 h of operation at -1.3 V (*vs.* SCE) with 100 mg/L NO_3^--N, the nitrate removal efficiencies were 100%, 56.7%, and 33.6% for Fe@Fe_3O_4/FF, Fe/FF, and Fe_3O_4/CC, respectively. This data indicates the superior efficacy of Fe@Fe_3O_4/FF in NO_3RR, outperforming the other tested cathodes. Of particular note, all NH_3 yield rates were normalized against the electrochemically active surface area (ECSA), which represents the maximum num-

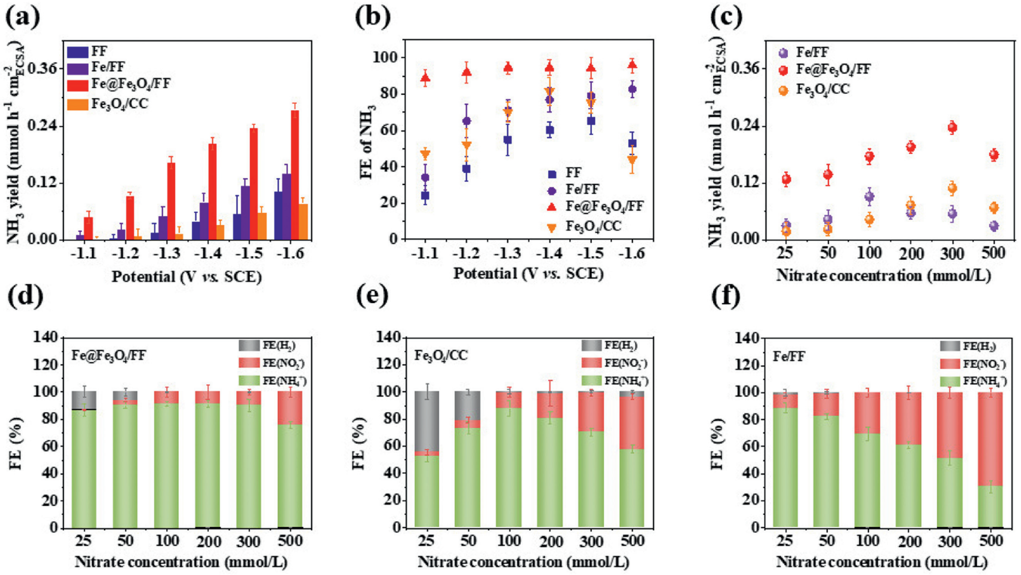

Fig. 2. Effects of applied potential on (a) NH_3 yield rate and (b) FE of NH_3, and (c) the impact of nitrate concentration on NH_3 yield rate across all the investigated cathodes. Nitrate concentration-dependent FE of various products during NO_3RR for (d) Fe@Fe_3O_4/FF, (e) Fe_3O_4/CC, and (f) Fe/FF. Unless otherwise specified, reaction conditions are as follows: applied potential of −1.3 V (*vs.* SCE), 100 mmol/L Na_2SO_4, 100 mmol/L $NaNO_3$, and 1 h of electrolysis.

ber of available active sites during electrolysis. The ECSA was measured using the well-established double-layer capacitance method, as detailed in Figs. S5 and S6 (Supporting information). As illustrated in Figs. 2a and b, the Fe@Fe_3O_4/FF cathode exhibited significantly higher NH_3 yield performance across all tested potentials compared to its counterparts. It is noticeable that the NH_3 yield rate for Fe@Fe_3O_4/FF increased progressively from 0.056 mmol h^{-1} cm^{-2} to 0.28 mmol h^{-1} cm^{-2} as the potential shifted more negatively from −1.1 V to −1.6 V (*vs.* SCE), achieving a high FE of 95.7% even at the high overpotential of −1.6 V (*vs.* SCE). This highlights the exceptional capability of Fe@Fe_3O_4/FF in facilitating NH_3 production *via* NO_3RR. In contrast, the peak NH_3 yield rates and FE at −1.6 V (*vs.* SCE) for the other cathodes were significantly lower, recording 0.10 mmol h^{-1} cm^{-2}/53.0%, 0.14 mmol h^{-1} cm^{-2}/82.7%, and 0.076 mmol h^{-1} cm^{-2}/44.1% for the FF, Fe/FF, and Fe_3O_4/CC, respectively, which were all markedly inferior to the performance of Fe@Fe_3O_4/FF. In addition, the NH_3 yield response to varying nitrate concentrations exhibited distinct patterns for Fe/FF, Fe_3O_4/CC, and Fe@Fe_3O_4/FF, as depicted in Fig. 2c, where each catalyst showed a volcano-shaped yield curve, albeit with different nitrate concentration turning points. The NH_3 yield rates for Fe_3O_4/CC and Fe@Fe_3O_4/FF followed a similar trend, increasing with nitrate concentration from 25 mmol/L to 300 mmol/L before showing a decline, with peak NH_3 yields of 0.11 mmol h^{-1} cm^{-2} and 0.23 mmol h^{-1} cm^{-2}, respectively. Fe/FF exhibited a decrease in the NH_3 yield rate at a lower nitrate concentration of 100 mmol/L, indicating its higher sensitivity to nitrate concentration. The suppression of NH_3 yield at high nitrate concentrations occurred likely because the nitrite produced could not be continuously reduced to ammonia. This was due to the high concentration of nitrate in the bulk solution, which competed with the intermediate nitrite for electrons on the cathode.

As illustrated in Figs. 2d-f, a remarkable increase in the accumulation of the undesired nitrite byproduct was observed for Fe/FF, with the FE(NO_2^-) values increasing across nitrate concentrations, reaching up to 69.3% at 500 mmol/L nitrate and −1.3 V (*vs.* SCE). Meanwhile, the maximum FE(NO_2^-) for Fe@Fe_3O_4/FF and Fe_3O_4/CC was significantly lower, indicating a more controlled nitrite formation during NO_3RR, especially at elevated nitrate concentrations. The values of FE(H_2) resulting from the competitive HER were also examined. It is revealed that this competitive reaction predominantly occurred at lower nitrate concentrations, with the Fe_3O_4/CC cathode more inclined towards favoring HER. Specifically, at 25 mmol/L nitrate, the FE(H_2) values were ranked as follows: Fe_3O_4/CC (44.42%) > Fe@Fe_3O_4/FF (13%) > Fe/FF (2%). Overall, the FE(NH_3) of Fe@Fe_3O_4/FF outperformed Fe_3O_4/CC and Fe/FF under all tested conditions, highlighting its superior ability for the selective production of NH_3.

Comprehensive evidence was presented to elucidate the mechanism underlying the exceptional performance of Fe@Fe_3O_4/FF in NO_3RR, particularly its remarkable NH_3 yield and substantially decreased nitrite production. The analysis involved three cathodes, Fe@Fe_3O_4/FF, Fe/FF, and Fe_3O_4/CC, and a control electrode, Fe_3O_4/nickel foam (NF), which was prepared in a manner analogous to Fe_3O_4/CC but utilized NF as the substrate. Figs. 3a-c and Fig. S7 (Supporting information) show the effects of tertiary butanol (TBA), a recognized scavenger of $^{\bullet}H$, on the linear sweep voltammetry (LSV) responses of various electrodes. The differences in current density reduction observed in the LSV curves upon the addition of TBA implied the varied influence of $^{\bullet}H$ in NO_3RR among various electrodes. Specifically, Fe@Fe_3O_4/FF exhibited a reduction in current density from 12.32 mA/cm^2 to 10.93 mA/cm^2 at −1.3 V (*vs.* SCE) in the presence of TBA, indicating a current density inhibition of 10.1%. Meanwhile, the suppression ratios of current density after TBA addition for the other electrodes were significantly higher, at 45.2% for Fe/FF, 77.4% for Fe_3O_4/CC, and 84.7% for Fe_3O_4/NF, respectively. This differential response suggests a predominant role of $^{\bullet}H$ in the NO_3RR for these electrodes, while DET may primarily facilitate NO_3RR on Fe@Fe_3O_4/FF.

Further investigation into the reaction mechanisms focused on evaluating nitrate removal efficiency in the presence of varying concentrations of TBA. Fig. 3d shows that Fe@Fe_3O_4/FF had minimal sensitivity to changes in TBA concentration, with removal efficiency slightly diminishing from 99.5% to 80.2% as the molar ratio of TBA to nitrate ($C_{(TBA)}/C_{(N)}$) was elevated from 0 to 50. This modest decline suggests a relatively low $^{\bullet}H$ contribution of 19.4% to the NO_3RR process for Fe@Fe_3O_4/FF, as illustrated in Fig. 3e. In contrast, the other electrodes experienced a more marked decrease in nitrate removal efficiency with the same increase in TBA concentration, with efficiencies dropping to 59.9%, 38.0%, and 19.5%

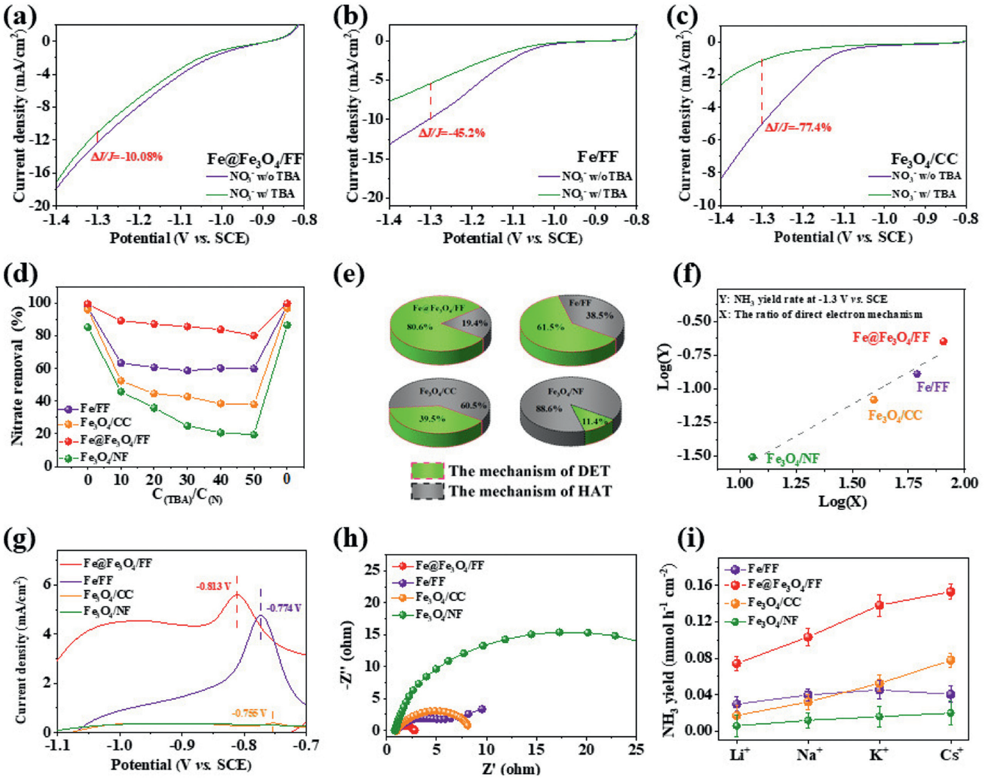

Fig. 3. Current density variations in LSV for (a) Fe@Fe_3O_4/FF, (b) Fe/FF, and (c) Fe_3O_4/CC electrodes following the addition of 300 mmol/L TBA and 100 mg/L $NaNO_3$. (d) Impact of TBA concentration on the nitrate removal efficiency across four electrodes, and (e) corresponding calculations of the contributions from different mechanisms involved in NO_3RR. (f) Correlation between the NH_3 yield rate and the proportion of DET in NO_3RR, as determined from (e). (g) Measurement of the OH^- adsorptive peak in 1 mol/L NaOH solution. (h) EIS spectra of the three electrodes at −1.1 V (*vs.* SCE) in the presence of 100 mg/L $NaNO_3$. (i) Influence of different alkali metal cations in the electrolyte on the NH_3 yield rate for the three electrodes, evaluated in a solution of 100 mmol/L M_2SO_4 and 100 mmol/L MNO_3 at −1.3 V (*vs.* SCE).

for Fe/FF, Fe_3O_4/CC, and Fe_3O_4/NF, respectively. This pattern, coupled with the distinct reduction in current density observed in LSV curves after TBA was added, infers $^\bullet$H contributions of 38.5%, 60.5%, and 88.6% to NO_3RR for Fe/FF, Fe_3O_4/CC, and Fe_3O_4/NF, respectively. In addition, after performing reactions with a $C_{(TBA)}/C_{(N)}$ ratio of 50 for all electrodes, the nitrate removal efficiency was reevaluated without the addition of TBA. Interestingly, the reassessment resulted in efficiency values that were almost identical to those recorded in the initial tests under the same conditions for all electrodes. This consistency indicates that the inhibitory effect of TBA stems from its scavenging activity rather than a poisoning effect on the electrodes [25,26]. This conclusion highlights the distinctive pathways through which each electrode facilitates NO_3RR, with Fe@Fe_3O_4/FF exhibiting a particularly efficient and less $^\bullet$H-dependent reaction mechanism.

The ESR technology was utilized to semi-quantitatively measure the amount of electrochemically generated $^\bullet$H across the four electrodes under identical conditions. As illustrated in Fig. S8 (Supporting information), the characteristic peaks for 5,5-dimethyl-1-pyrroline N-oxide (DMPO)-$^\bullet$H, a marker for $^\bullet$H, were detected for all four electrodes, albeit with varying signal intensities. Fe_3O_4/NF exhibited the highest peak intensity of DMPO-$^\bullet$H, followed by Fe_3O_4/CC, Fe/FF, and Fe@Fe_3O_4/FF, respectively. This order aligns with the previously determined $^\bullet$H contributions to the NO_3RR, again delineating the different predominant reaction mechanisms for each electrode. Combining these findings with earlier experimental results, it is conclusively determined that Fe@Fe_3O_4/FF primarily facilitates NO_3RR *via* the DET mechanism. In contrast, HAT predominantly drives the reaction for Fe_3O_4/CC and Fe_3O_4/NF, while both DET and HAT mechanisms are active in Fe/FF. Intriguingly, when correlating the NH_3 yield rate *via* NO_3RR at −1.3 V (*vs.* SCE) with the contribution of the DET mechanism, a nearly linear relationship appeared (Fig. 3f). This suggests that the superior NH_3 yield rate and substantially reduced nitrite production observed for Fe@Fe_3O_4/FF may be attributed to the dominance of the DET mechanism and minimal involvement of HAT. Therefore, a significant contribution from the DET mechanism is fundamentally crucial for the exceptional performance of Fe@Fe_3O_4/FF in achieving high NH_3 generation.

Based on the established relationship between reaction mechanisms and NO_3RR performance, the next step was to elucidate how the inherent properties of electrocatalysts influence these mechanisms. It is hypothesized that the strong adsorption of NO_3^- and other nitrogen-containing intermediates onto the surface of electrocatalysts is crucial for the NO_3RR to proceed *via* the DET mechanism [20,27,28], thereby leading to enhanced NO_3RR performance. To test this hypothesis, the adsorption of OH^- serving as a proxy for NO_3^- and other nitrogen-containing intermediates generated during NO_3RR was measured using the cyclic voltammetry (CV) technology. The results in Fig. 3g show that Fe@Fe_3O_4/FF exhibited the strongest OH^- adsorption, as indicated by the most negative potential of the OH^- adsorptive peak at −0.813 V (*vs.* SCE). This suggests a potentially strong bond between nitrogen-containing species and Fe@Fe_3O_4/FF, facilitating direct electron transfer. In comparison, the OH^- adsorptive peaks for Fe/FF and Fe_3O_4/CC were observed at −0.774 and −0.755 V (*vs.* SCE), respectively, indicating a better adsorption affinity for nitrogen-containing species on Fe/FF than on Fe_3O_4/CC, but still inferior to Fe@Fe_3O_4/FF. No peak corresponding to OH^- adsorption was detected on Fe_3O_4/NF, indicating inferior nitrate adsorption for Fe_3O_4/NF. The measured order of OH^- adsorptive peak potentials correlated well with the contribution of the DET mechanism

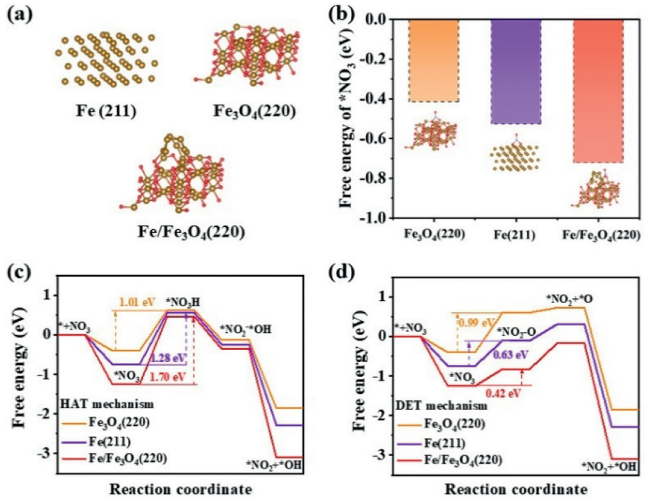

Fig. 4. (a) Representations of Fe/FF, Fe_3O_4/CC, and Fe@Fe_3O_4/FF models used for theoretical calculations. (b) Comparative analysis of $NO_3{}^-$ adsorption free energy across the three models. Evaluation of the kinetic energy barrier for (c) HAT and (d) DET mechanisms on each of the models.

in NO_3RR for the electrodes, suggesting that enhanced adsorption of nitrogen-containing species is favorable for NO_3RR *via* the DET mechanism. Moreover, the interfacial charge transfer resistance for Fe@Fe_3O_4/FF, Fe/FF, Fe_3O_4/CC and Fe_3O_4/NF was determined using electrochemical impedance spectroscopy (EIS) (Fig. 3h). As anticipated, Fe@Fe_3O_4/FF displayed the lowest resistance to charge transfer, as evidenced by the smallest diameter of the corresponding semi-circle in the EIS spectra. This result supports the most favorable interfacial electron transfer for Fe@Fe_3O_4/FF, followed by Fe/FF, Fe_3O_4/CC and Fe_3O_4/NF, and aligns with the previously mentioned contribution of the DET mechanism in NO_3RR.

The role of protonation kinetics, alongside enhanced adsorption of nitrogen-containing species, is also crucial for achieving high NH_3 yield, especially given the nature of electrochemical hydrogenation in aqueous media. This study examined the protonation kinetics of three electrocatalysts by altering the alkali metal cation of the electrolyte from Li^+ to Na^+, K^+, and Cs^+, a method thoroughly documented in existing literature [29-31]. Fig. 3i shows that Fe@Fe_3O_4/FF, Fe_3O_4/CC, and Fe_3O_4/NF all exhibited progressively improved NH_3 yield rates with the transition from Li^+ to Cs^+, increasing from 0.074, 0.03, and 0.0058 $mmol\,h^{-1}\,cm^{-2}$ to 0.15, 0.08, and 0.02 $mmol\,h^{-1}\,cm^{-2}$, respectively. This improvement indicates the favorable protonation kinetics of Fe@Fe_3O_4/FF, Fe_3O_4/CC, and Fe_3O_4/NF, consistent with trends reported previously [30,32]. In contrast, Fe/FF demonstrated a minimal improvement in NH_3 yield rate, from $mmol\,h^{-1}\,cm^{-2}$ 0.03 to 0.04 $mmol\,h^{-1}\,cm^{-2}$ under the same conditions, indicating weaker protonation kinetics and manifesting the critical role of Fe_3O_4 in enhancing NO_3RR protonation. Interestingly, the superior protonation kinetics of Fe@Fe_3O_4/FF and Fe_3O_4/CC were closely associated with a significantly reduced accumulation of nitrite, as observed in Figs. 2d-f. This suggests that the presence of Fe_3O_4 in these electrocatalysts facilitates the continuous protonation of intermediate nitrite into NH_3. This effect is likely due to the inherent ability of common metal oxides, such as Fe_3O_4, to adsorb and dissociate water effectively [33,34].

DFT calculations were employed to deepen the understanding of the relationship between catalyst structure and NO_3RR performance, particularly focusing on the advantages of the DET mechanism over the HAT mechanism. Three representative models (Fig. 4a), Fe(211) for Fe/FF, $Fe_3O_4(220)$ for Fe_3O_4/CC, and Fe@$Fe_3O_4(220)$ for Fe@Fe_3O_4/FF, were developed based on the experimental characterizations presented in Fig. 1, to closely reflect the structures of the actual catalysts. The adsorption free energy of $NO_3{}^-$ on these models was calculated to identify which structure favored $NO_3{}^-$ binding, a significant aspect in determining the reaction mechanism [35]. The results, shown in Fig. 4b, indicate that Fe@$Fe_3O_4(220)$ exhibited the highest ΔG for $NO_3{}^-$ adsorption at -0.772 eV, followed by -0.526 eV for Fe(221) and -0.415 eV for $Fe_3O_4(220)$. This suggests that the Fe component in Fe@Fe_3O_4/FF plays a pivotal role in enhancing $NO_3{}^-$ adsorption, thereby contributing to its superior NO_3RR performance. The slightly stronger $NO_3{}^-$ adsorption on Fe@$Fe_3O_4(220)$ compared to Fe(221) also highlighted the beneficial effect of the coexisting Fe_3O_4 in Fe@Fe_3O_4/FF, aligning with the experimentally observed trends in $NO_3{}^-$ adsorption. In addition, the kinetic energy barrier for the initial step of NO_3RR ($NO_3{}^- \rightarrow NO_2{}^-$), often considered the rate-limiting step [36], was evaluated for both HAT and DET mechanisms. The HAT mechanism involves the direct hydrogenation of adsorbed $NO_3{}^-$ ($*NO_3$) by adjacent $^{\bullet}H$, while DET facilitates this transformation through sequential proton and electron transfer to adsorbed $NO_3{}^-$ without the involvement of neutral $^{\bullet}H$. The energy profiles for $NO_3{}^-$ transformation into $NO_2{}^- + OH^-$ *via* both mechanisms were analyzed for all three models (Figs. 4c and d). Notably, $Fe_3O_4(220)$ exhibited the lowest energy barrier of 1.01 eV for the HAT mechanism, followed by 1.28 eV for Fe(221) and 1.70 eV for Fe@$Fe_3O_4(220)$, consistent with the experimentally measured contributions of the HAT mechanism. Conversely, Fe@$Fe_3O_4(220)$ presented the lowest energy barrier of 0.42 eV for the DET mechanism, followed by 0.63 eV for Fe(221) and 0.99 eV for $Fe_3O_4(220)$, theoretically supporting the preference for NO_3RR *via* DET on Fe@Fe_3O_4/FF and suggesting a significant contribution of the HAT mechanism for NO_3RR over Fe_3O_4/CC. These theoretical outcomes confirm the DET mechanism's favorable position relative to the HAT mechanism, especially since Fe@Fe_3O_4/FF, dominated by DET, exhibited the best nitrate conversion capability among the three investigated electrodes. This comprehensive analysis not only corroborates the experimental observations but also provides a mechanistic understanding of why Fe@Fe_3O_4/FF outperforms its counterparts in NO_3RR, highlighting the critical role of catalyst structure in dictating the reaction pathway and efficiency.

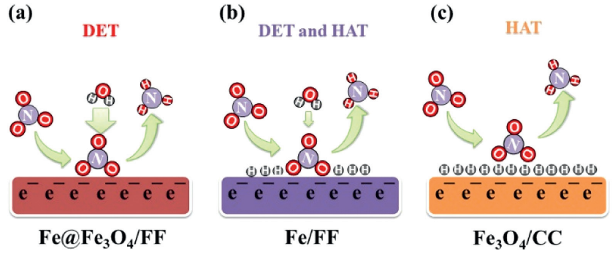

Fig. 5. Schematic representation of reaction mechanisms on (a) Fe@Fe_3O_4/FF, (b) Fe/FF, and (c) Fe_3O_4/CC.

The collaborative experimental and theoretical analyses provided profound insights into the mechanics and effects of different components within electrocatalysts on NO_3RR. Fig. 5 encapsulates these insights, highlighting how the interplay between metallic Fe and Fe_3O_4 within Fe@Fe_3O_4/FF enhances the NO_3RR process. The role of metallic Fe is pivotal due to its strong adsorption capabilities for nitrogen-containing species, facilitated by intensive D-π interactions between the electron-rich metallic Fe surface and N atoms [37]. This interaction fosters a preference for the DET mechanism in NO_3RR, attributed to reduced interfacial resistance for charge transfer. Concurrently, the inclusion of Fe_3O_4 in Fe@Fe_3O_4/FF is advantageous for promoting favorable protonation kinetics, thanks to its high affinity for water adsorption and dissociation. This is attributed to the strong interaction between the empty d orbitals of the metal oxide and the lone-pair electrons of the oxygen atom in water molecules [33,38]. This characteristic significantly mitigates nitrite accumulation and boosts NH_3 production. In contrast, while Fe/FF also demonstrates robust nitrogen-containing species binding and low interfacial charge transfer resistance, its sole reliance on metallic Fe without the presence of Fe_3O_4 limits its protonation kinetics. This limitation could lead to considerable nitrite accumulation, especially at higher nitrate concentrations. Fe_3O_4/CC, characterized by effective protonation kinetics, however, exhibits poor NH_3 yield and slightly reduced nitrite accumulation, primarily influenced by the HAT mechanism. Therefore, the synergy between Fe and Fe_3O_4 in Fe@Fe_3O_4/FF is crucial for achieving superior NH_3 yield through the DET mechanism. This insight is useful for the design and development of highly effective electrocatalysts for NO_3RR, emphasizing the need to balance components that enhance nitrogen-containing species adsorption and promote efficient protonation kinetics to minimize undesirable byproducts and maximize desired outcomes.

The performance of Fe@Fe_3O_4/FF for complete denitrification under various conditions, including the presence of NaCl, was thoroughly assessed. The addition of NaCl aimed to initiate electrochemically mediated breakpoint chlorination, oxidizing the NH_4^+ generated from NO_3RR into harmless N_2 [39-42]. Fig. S9a (Supporting information) shows that 500 mg/L NO_3^--N can be fully removed at 30 mA/cm^2 after 3 h of electrolysis, achieving a *pseudo*-first-order rate constant of 1.39 h^{-1}. This rate constant was observed to increase incrementally to 1.43, 1.49, and 1.52 h^{-1} as the current density was raised to 35, 40, and 45 mA/cm^2, respectively. Negligible amounts of NH_4^+-N and NO_2^--N were detected after the electrolysis process, indicating the capability of Fe@Fe_3O_4/FF for complete denitrification with the assistance of NaCl.

The impacts of initial NO_3^--N concentration and NaCl concentration on the denitrification efficiency of Fe@Fe_3O_4/FF were explored, as presented in Figs. S9b and c (Supporting information). An observed trend showed a gradual decline in the kinetics as the initial NO_3^--N concentration increased from 500 mg/L to 800 mg/L, attributed to the limitation in active sites [43]. Nevertheless, nearly 100% denitrification efficiency was still achieved after 3 h of electrolysis, even at the elevated NO_3^--N concentration of 800 mg/L. Complete removal of 500 mg/L NO_3^--N was observed, irrespective of the NaCl amount. The denitrification kinetics exhibited a slight improvement with increasing concentrations of NaCl. This enhancement may be attributed to the refreshment of active sites occupied by the NH_3 product and the alleviation of pH increase in the solution through electrochemically mediated breakpoint chlorination. This suggests a strong resistance to oxidative corrosion by active chlorine species produced from Cl$^-$ oxidation at the anode [41,42]. The Fe@Fe_3O_4/FF cathode maintained exceptional denitrification efficiency across a pH range from 7 to 12 (Fig. S9d in Supporting information), suggesting the promising potential for practical applications. The acidic conditions were not examined in the present study due to inevitable dissolution of Fe_3O_4 under these conditions. Material stability, a critical performance metric, was evaluated over 20 cycles. As shown in Fig. S10 (Supporting information), the Fe@Fe_3O_4/FF cathode showed consistent denitrification efficiency of approximately 100% removal across all cycles, indicating its exceptional robustness. The post-XRD pattern of Fe@Fe_3O_4/FF in Fig. S11 (Supporting information) displayed a profile similar to that of the pristine Fe@Fe_3O_4/FF. These findings highlight the effectiveness and durability of Fe@Fe_3O_4/FF in complex water treatment scenarios, offering a promising approach to achieving complete denitrification in the presence of challenging constituents like NaCl.

Given the advantages of Fe@Fe_3O_4/FF, such as cost-effectiveness and ease of scale-up, the practical feasibility of using Fe@Fe_3O_4/FF as a cathode material for treating real wastewater with high nitrate concentrations was investigated. To facilitate complete denitrification through electrochemically mediated breakpoint chlorination, an additional 100 mmol/L NaCl was supplemented into the wastewater. An experimental setup featuring an internal circulation mode was constructed, as depicted in Fig. S12a (Supporting information). This setup was operated in an internal-circulation mode, including a peristaltic pump for flow rate control, an electrolyzer equipped with a larger-sized Fe@Fe_3O_4/FF cathode (4 cm × 3 cm) for denitrification, and a container for storing and mixing 500 mL of the original wastewater with the effluent from the electrolyzer. Operating at a current density of 30 mA/cm^2 and a flow rate of 1 mL/min, the NO_3^--N concentration in the wastewater was steadily reduced from 3815 mg/L to zero over 120 h of electrolysis, as shown in Fig. S12b (Supporting information). The byproducts of NH_4^+-N and NO_2^--N were scarcely accumulated by the end of the process, demonstrating the effectiveness of active chlorine species generated from Cl$^-$ oxidation at the MMO anode in ensuring efficient denitrification. In stark contrast, when using Fe/FF as the cathode under identical operating conditions, the denitrification performance was significantly inferior, achieving only a 29.3% removal efficiency.

In conclusion, through detailed investigations of NO_3RR on Fe/FF, Fe_3O_4/CC, and Fe@Fe_3O_4/FF cathodes, we have clearly established that the catalyst structure directly influences the reaction mechanism and, consequently, the NO_3RR performance. The Fe@Fe_3O_4/FF cathode demonstrated a strong affinity for NO_3^- and a moderate capability for water dissociation, being attributed to its metallic Fe and Fe_3O_4 components, respectively. These characteristics are key to the preferred occurrence of the DET mechanism during NO_3RR, leading to the outstanding denitrification performance of Fe@Fe_3O_4/FF. Conversely, the absence of metallic oxide Fe_3O_4 in Fe/FF, which is crucial for the protonation process, resulted in poor NO_3RR performance and significant accumulation of the intermediate product nitrite. Fe_3O_4/CC, containing only the metallic oxide Fe_3O_4 component, exhibited inferior denitrification performance. The lack of metallic Fe, which is essential for strong bonding with NO_3^-, leads to a preference for the HAT mechanism during NO_3RR. This preference accelerates the competitive HER and limits denitrification performance, despite a noticeable reduction in the accumulation of NO_2^- due to the enhanced protonation capability of Fe_3O_4. These experimental insights are crucial for a fundamental understanding of the DET and HAT mechanisms involved in NO_3RR. They also provide a solid foundation for the rational design and development of advanced catalysts for effective nitrate reduction, highlighting the importance of carefully considering catalyst composition and structure to optimize performance.

Declaration of competing interest

The authors declare that they have no known competing financial interests or personal relationships that could have appeared to influence the work reported in this paper.

CRediT authorship contribution statement

Yuwei Liu: Writing – original draft, Investigation, Formal analysis, Data curation. **Yihui Zhu:** Investigation, Formal analysis, Data curation. **Weijian Duan:** Writing – original draft, Methodology, Data curation, Conceptualization. **Yizhuo Yang:** Resources, Data curation. **Haorui Tuo:** Investigation, Data curation. **Chunhua Feng:** Writing – review & editing, Supervision, Methodology, Formal analysis, Conceptualization.

Acknowledgments

We gratefully acknowledge financial support from the National Natural Science Foundation of China (Nos. U21A2034 and

21876052), the Guangdong Special Support Plan for Innovation Teams (No. 2019BT02L218), the Guangdong Special Support Plan for Young Top-notch Talents (No. 2019TQ05L179), and the Natural Science Foundation of Guangdong Province, China (No. 2021B1515120077).

Supplementary materials

Supplementary material associated with this article can be found, in the online version, at doi:10.1016/j.cclet.2024.110347.

References

[1] M. Duca, M.T.M. Koper, Energy Environ. Sci. 5 (2012) 9726–9742.
[2] H. Xu, Y. Ma, J. Chen, W.X. Zhang, J. Yang, Chem. Soc. Rev. 51 (2022) 2710–2758.
[3] Y. Xiong, Y. Wang, J. Zhou, et al., Adv. Mater. 36 (2024) 2304021.
[4] Y. Wang, C. Wang, M. Li, Y. Yu, B. Zhang, Chem. Soc. Rev. 50 (2021) 6720–6733.
[5] W. Zheng, L. Zhu, Z. Yan, et al., Environ. Sci. Technol. 55 (2021) 13231–13243.
[6] T. Zhu, Q. Chen, P. Liao, et al., Small 16 (2020) 2004526.
[7] Y. Ren, S. You, Y. Wang, J. Yang, Y. Liu, Environ. Sci. Technol. 58 (2024) 2144–2152.
[8] J. Guo, P. Chen, Chem 3 (2017) 709–712.
[9] J. Li, G. Zhan, J. Yang, et al., J. Am. Chem. Soc. 142 (2020) 7036–7046.
[10] M. Fu, Y. Mao, H. Wang, et al., Chin. Chem. Lett. 35 (2024) 108341.
[11] Y. Xu, K. Shi, T. Ren, et al., Small 18 (2022) 2203335.
[12] Y. Wang, A. Xu, Z. Wang, et al., J. Am. Chem. Soc. 142 (2020) 5702–5708.
[13] H. Yin, X. Mao, S. Bell, D. Golberg, A. Du, Chem. Mater. 35 (2023) 2884–2891.
[14] X. Fan, L. Xie, J. Liang, et al., Nano Res. 15 (2022) 3050–3055.
[15] L. Fang, S. Wang, S. Lu, et al., Chin. Chem. Lett. 35 (2024) 108864.
[16] Z.Y. Wu, M. Karamad, X. Yong, et al., Nat. Commun. 12 (2021) 2870.
[17] X.F. Cheng, J.H. He, H.Q. Ji, et al., Adv. Mater. 34 (2022) 2205767.
[18] Y. Xue, Q. Yu, Q. Ma, et al., Environ. Sci. Technol. 56 (2022) 14797–14807.
[19] J. Gao, B. Jiang, C. Ni, et al., Appl. Catal. B 254 (2019) 391–402.
[20] Y. Li, J. Ma, Z. Wu, Z. Wang, Environ. Sci. Technol. 56 (2022) 8673–8681.
[21] X. Li, P. Shen, X. Li, D. Ma, K. Chu, ACS Nano 17 (2023) 1081–1090.
[22] N. Zhang, G. Zhang, P. Shen, et al., Adv. Funct. Mater. 33 (2023) 2211537.
[23] K. Fan, W. Xie, J. Li, et al., Nat. Commun. 13 (2022) 7958.
[24] W. Duan, Y. Chen, H. Ma, et al., Environ. Sci. Technol. 57 (2023) 3893–3904.
[25] R. Mao, N. Li, H. Lan, et al., Environ. Sci. Technol. 50 (2016) 3829–3837.
[26] H. Lan, R. Mao, Y. Tong, et al., Environ. Sci. Technol. 50 (2016) 11872–11878.
[27] W. Fu, Y. Du, J. Jing, C. Fu, M. Zhou, Appl. Catal. B 324 (2023) 122201.
[28] X. Zhao, Y. Jiang, M. Wang, et al., Adv. Energy Mater. 13 (2023) 2301409.
[29] S. Xue, B. Garlyyev, S. Watzele, et al., ChemElectroChem 5 (2018) 2326–2329.
[30] W. Ma, S. Xie, T. Liu, et al., Nat. Catal. 3 (2020) 478–487.
[31] X. Lu, W. Tu, Y. Zhou, Z. Zou, Adv. Energy Mater. 13 (2023) 2300628.
[32] W. Ma, S. Xie, X.G. Zhang, et al., Nat. Commun. 10 (2019) 892.
[33] H. Sun, Z. Yan, C. Tian, et al., Nat. Commun. 13 (2022) 3857.
[34] K.L. Zhou, Z. Wang, C.B. Han, et al., Nat. Commun. 12 (2021) 3783.
[35] Y. Hua, N. Song, Z. Wu, et al., Adv. Funct. Mater. 34 (2024) 2314461.
[36] H. Jiang, G.F. Chen, O. Savateev, et al., Wang, Angew. Chem. Int. Ed. 62 (2023) 18717.
[37] Y. Dong, J.B. Chen, J. Ying, et al., Chem. Mater. 34 (2022) 8271–8279.
[38] W. Shen, Y. Zheng, Y. Hu, et al., J. Am. Chem. Soc. 146 (2024) 5324–5332.
[39] Z. Yan, W.J. Kuang, Y. Lei, et al., Environ. Sci. Technol. 57 (2023) 20915–20928.
[40] C. Zhang, D. He, J. Ma, T.D. Waite, Water Res. 145 (2018) 220–230.
[41] F. Li, L. Sun, Y. Liu, et al., J. Hazard. Mater. 400 (2020) 123246.
[42] F. Li, X. Peng, Y. Liu, et al., Chemosphere 229 (2019) 383–391.
[43] Z.Y. Wu, P. Zhu, D.A. Cullen, et al., Nat. Synth. 1 (2022) 658–667.